Carbon 126 (2018) 17–22

Contents lists available at ScienceDirect

Carbon

journal homepage: www.elsevier.com/locate/carbon

Extenuated interlayer scattering in double-layered graphene/hexagonal boron nitride heterostructure

Nikhil Jain [a], Fan Yang [a], Robin B. Jacobs-Gedrim [a], Xu Xu [b], M.P. Anantram [b], Bin Yu [a, *]

[a] College of Nanoscale Science and Engineering State University of New York, Albany, NY, 12203, USA
[b] Department of Electrical Engineering University of Washington, Seattle, WA, 98195, USA

ARTICLE INFO

Article history:
Received 24 April 2017
Received in revised form
15 September 2017
Accepted 18 September 2017
Available online 18 September 2017

ABSTRACT

Interlayer carrier scattering hampers electrical conduction in two-dimensional layered nanostructures. Extenuated carrier scattering is observed in a double-layered graphene system with hexagonal boron nitride (*h*-BN) as an interposer. Raman spectrum shows signature peaks with enhanced sharpness as compared with that of bilayer graphene. The density functional theory simulation shows degenerate energy bands in the *E-k* dispersion. The decoupling of the two graphene monolayers is further confirmed by electrical conduction measurements. Improved carrier mobility is observed in the graphene/*h*-BN/graphene heterostructure as compared with exfoliated or randomly-stacked graphene bilayer, indicating preserved Fermi velocity. The demonstrated behavior in graphene/*h*-BN/graphene heterostructure suggests a pathway to preserve the excellent carrier transport of pristine graphene monolayer in a multi-channel configuration, leading to implementation of highly conductive 2D heterostructure systems.

© 2017 Elsevier Ltd. All rights reserved.

1. Introduction

Pristine graphene in its monolayer form exhibits superb electrical [1–3], mechanical [4–6], and electromechanical behaviors [7–9]. Monolayer graphene possesses ~100 times higher current density than copper [10], demonstrating potential in future-generation interconnect and wiring applications. However, its one-atom-thick configuration means extremely-small cross-sectional area, limiting current-carrying capacity. Research efforts on bilayer and multilayer graphene (stacked in *AB* Bernal configuration [11] or with random pattern [12,13]) have indicated reduced conductivity with increasing layer number due to non-linear *E-k* dispersion [14]. Additionally, carrier coupling in the adjacent monolayers results in degraded conduction, as reflected in interlayer resistance [15]. Randomly-stacked (known as *turbostratic*) graphene has been reported to exhibit lesser interlayer coupling, as compared to *AB*-stacked bilayer, due to decoupling of the monolayers. This is believed to be caused by carrier momentum conservation, confirmed by the linear dispersion at low-energy regime near the Dirac point [16–19]. However, considerably reduced Fermi velocity is observed in turbostratic bilayer graphene, as comparison with that in monolayer, indicating undesirable impact of the adjacent layer on carrier transport [20,21].

It has been demonstrated that, when individual monolayers are decoupled, the carriers in graphene multilayer continue to behave as massless Dirac fermions, and each layer can be viewed as independent [22]. The turbostratic bilayer, comprised of two monolayers randomly stacked over each other, allows for mitigated interlayer coupling which leads to improved conduction than *AB*-stacked bilayer. However, interlayer scattering is observed in turbostratic bilayer, as seen from velocity renormalization [23]. This leads to degraded carrier mobility. The phonon-mediated conductance arises primarily from the vibrational beating mode of the bilayer, in which out-of-plane acoustic (flexural) modes of the two layers are 180° out of phase, such that the layers vibrate against each other. For any rotational angle, carrier scattering can be significant at room temperature, resulting in compromised electrical conductivity.

In this work we study the conducting behavior in a double-layered graphene system. Two-dimensional (2D) dielectric, hexagonal boron nitride (*h*-BN), is used as an intercalating layer sandwiched between two graphene monolayers. This yields graphene/*h*-BN/graphene (G/*h*-BN/G) heterostructure which serves as the unit cell in graphene/*h*-BN superlattice-like structure. The selection of *h*-BN as interposing layer is rational due to its atomically smooth, self-terminated surfaces, along with its high optical

* Corresponding author.
E-mail address: byu@sunypoly.edu (B. Yu).

https://doi.org/10.1016/j.carbon.2017.09.074
0008-6223/© 2017 Elsevier Ltd. All rights reserved.

phonon energy (~2.5 times that in SiO_2), all contributing to the preservation of carrier transport in graphene [24–27].

2. Experiment

Preparation of graphene/h-BN/graphene samples. Monolayer graphene was grown on copper foil and transferred onto Si/SiO_2 substrate using the PMMA/iron chloride assisted technique. Graphene was then patterned with e-beam lithography (Vistec VB 300) and excessive graphene was etched away with O_2 plasma-based RIE (Micro-RIE). The process was described in detail in prior publication [25]. Graphene monolayer was patterned into 1 μm × 5 μm ribbon, followed by transferring a 3 μm-wide *h*-BN multilayer (~22 nm thick, measured from AFM). Another graphene monolayer was subsequently transferred and patterned to nearly the same size as the first one. Top metal contacts were made with 5 nm Ti/40 nm Au stack. The resultant structure is a 1 μm × 3 μm strip of graphene/*h*-BN/graphene heterostructure.

Electrical measurements. The samples were annealed overnight at 300 °C in forming gas to minimize hysteretic effect. All electrical characterization was performed in vacuum condition on Lakeshore Cryotronics probe station using Agilent B1500A semiconductor parameter analyzer.

3. Results and discussion

Fig. 1a shows the atomic-lattice schematic of graphene/*h*-BN/graphene heterostructure. Although *AB*-stacked pattern is given for illustrative, the stacking pattern in prepared sample is random. Fig. 1b is the optical image of the implemented structure with probing metal contacts. It was reported that, if different from 60°, twist angle in stacked bilayer has insignificant impact on interlayer coupling [16]. Fig. 1c is the schematic heterostructure with metal contacts, and Fig. 1d illustrates the contact at the edge of graphene layers. In the studied structure metal contacts only touch the bottom monolayer at its edges, while making top and edge contact with the upper monolayer [28]. Wang et al. reported that metal-graphene contact along the edge shows low resistance [29]. Fig. 1e shows the AFM scan of the *h*-BN flake used for making the heterostructure, confirming the flake thickness of 22 nm. Besides dual-layer graphene structure, CVD monolayer graphene, CVD stacked bilayer graphene, and exfoliated bilayer graphene were also compared in this experiment.

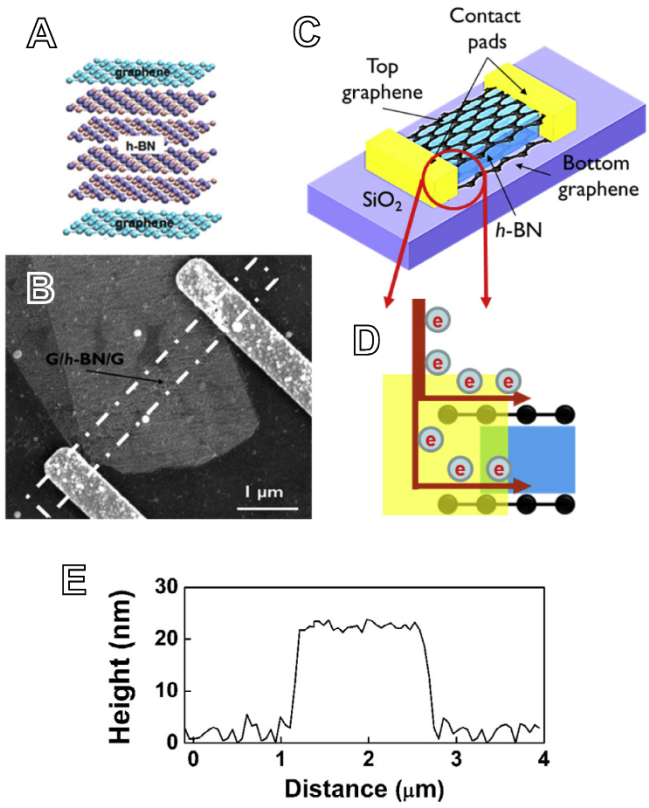


Fig. 1. **(a)** Atomic-lattice schematic of the double-layered graphene structure separated by a thin interposing *h*-BN multilayer; **(b)** SEM image showing the fabricated heterostructure with two probing contacts (Ti/Au). Here the dash-dotted lines show the edges of the plasma-etched graphene ribbon for eye-guiding purpose. **(c)** Schematic tilted-view of the graphene/*h*-BN/graphene heterostructure. **(d)** Zoomed-in view showing the detail of the graphene-metal contact. **(e)** AFM scanning results showing the thickness of *h*-BN as 22 nm. (A colour version of this figure can be viewed online.)

3.1. Raman spectrum analysis

We conducted Raman spectral analysis to investigate the influence of interposing *h*-BN on interlayer carrier scattering in a graphene/*h*-BN/graphene heterostructure. Fig. 2a shows the Raman spectrum generated from monolayer, exfoliated bilayer, stacked bilayer, and graphene/*h*-BN/graphene heterostructure. It should be noted that, as the growth and transfer process is the same for CVD graphene, the defect peak positioned at ~1350 cm^{-1} should be similar. Therefore, the sharp peak at 1365 cm^{-1} is the signature of *h*-BN layer. Other than that, the most noticeable difference is the sp^2 carbon G peak positioned at ~1583 cm^{-1} and double-resonance 2D peak at ~2700 cm^{-1}. Due to the presence of two phonon modes with opposite momentum in the highest optical branch, 2D band provides the information about layer number in few-layer graphene (FLG) [30]. The layer number in *AB*-stacked FLG is estimated from the intensity ratio of G peak to 2D peak, or I_G/I_{2D}, valid up to 4–5 layers. Additionally, the band-splitting depends on the relative orientation of stacked layers [31]. Interlayer scattering in bilayer and multilayer graphene induces band-splitting, which in turn has

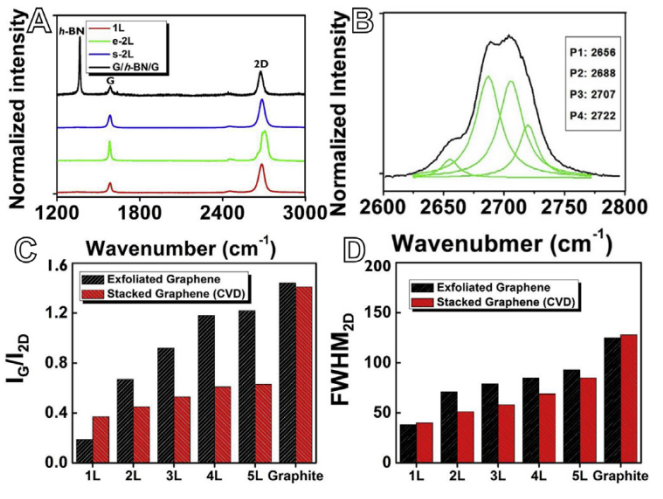


Fig. 2. **(a)** Intensity ratio of G-peak and 2D-peak as observed in Raman spectra measured on micromechanically exfoliated graphene and transferred-and-stacked CVD-graphene samples. **(b)** The full-width-at-half maximum of 2D peak in Raman spectra of graphene with different thickness. **(c)** Lorentzian curve-fitting of 2D peak of exfoliated graphene shows four components (P1-P4). The numbers in the inset are the corresponding values of wavenumber. **(d)** Raman spectra of graphene/*h*-BN/graphene heterostructure in comparison with that of CVD monolayer graphene (1L), exfoliated bilayer graphene (e-2L), and stacked dual-layer graphene (s-2L). (A colour version of this figure can be viewed online.)

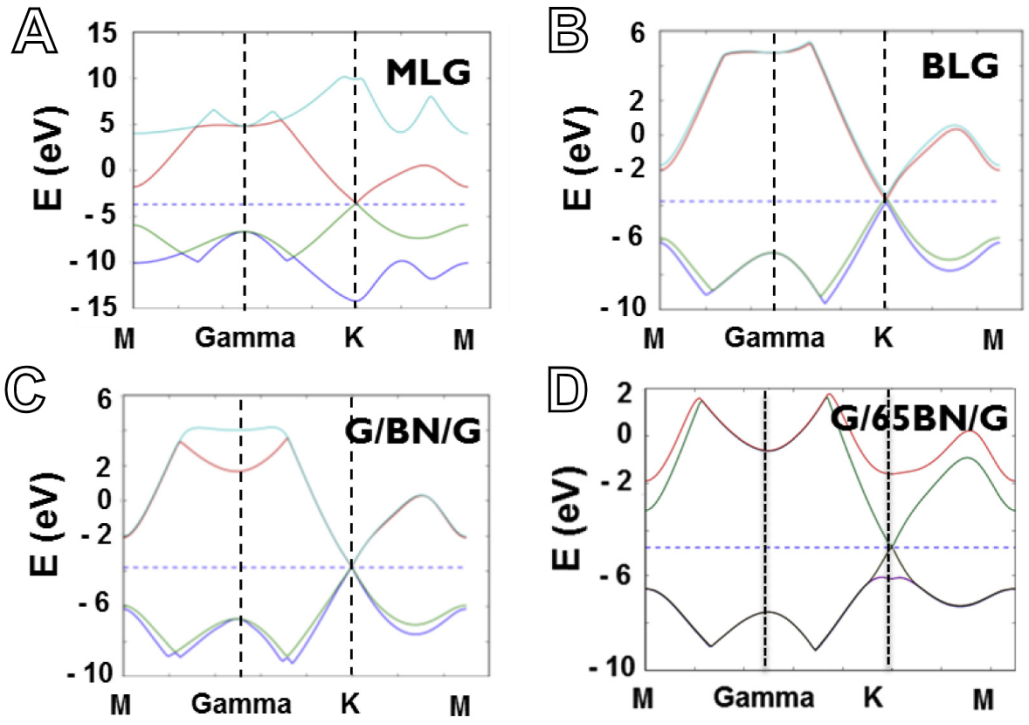


Fig. 3. Density-functional-theory simulation results of the *E-k* dispersion in four different configurations: **(a)** monolayer graphene, **(b)** *AB Bernal*-stacked bilayer graphene, **(c)** double-layered graphene with an interposing *h*-BN monolayer, and **(d)** double-layered graphene with an *h*-BN multilayer (22 nm thick). (A colour version of this figure can be viewed online.)

direct influence on the double resonance, leading to split 2D band. Thus, the 2D peak is lowered and broadened, increasing the full-width-at-half-maximum (FWHM). Lorentzian curve-fitting was used to isolate the individual 2D peak of the exfoliated bilayer. It consists of four components (2656 cm^{-1}, 2688 cm^{-1}, 2707 cm^{-1}, and 2722 cm^{-1}), as shown in Fig. 2b.

Peak intensity ratio and FWHM in the Raman spectra was extracted for one-to five-layer *AB* Bernal stacked (exfoliated) and turbostratic graphene, respectively, as illustrated in Fig. 2c and d. For exfoliated graphene, it is observed the I_G/I_{2D} ratio increases sharply from monolayer to bilayer, which is explained by the onset of interlayer scattering that creates 2D peak rounding. For turbostratic graphene, the disturbance in degeneracy ($I_G/I_{2D} = 0.45$) is not as much as in Bernal-stacked graphene ($I_G/I_{2D} = 0.67$), resulting in sharper 2D peak and lower I_G/I_{2D} ratio as observed in Fig. 2c. However, after adding *h*-BN interposing layer, the I_G/I_{2D} value is 0.39, close to that of a CVD monolayer graphene ($I_G/I_{2D} = 0.37$). The lowered ratio indicates reduced carrier scattering effect between the two graphene layers.

Further, it is seen in Fig. 2d that $FWHM_{2D}$ for exfoliated bilayer is nearly twice that of monolayer. Similarly, increased I_G/I_{2D} ratio is observed on exfoliated graphene with increasing layer number. For CVD graphene monolayer, the observed I_G/I_{2D} ratio and $FWHM_{2D}$ ($FWHM_{2D} = 40$ cm^{-1}) are higher than that of exfoliated monolayer ($FWHM_{2D} = 30$ cm^{-1}), which could be attributed to good crystallinity of exfoliated graphene. However, when two CVD graphene monolayers are stacked, the increase in I_G/I_{2D} ratio is less ($FWHM_{2D} = 51$ cm^{-1} as compared to exfoliated bilayer of 71 cm^{-1}), attributed to the extenuated interlayer scattering. This is evidenced by smaller change in $FWHM_{2D}$ in stacked bilayer. Additionally, it is seen that further addition of monolayers does not increase I_G/I_{2D} ratio as much as seen in the exfoliated sample. The impact on $FWHM_{2D}$ is also less significant, indicating less 2D peak broadening. This confirms that 2D peak broadening is an indication of layer coupling in multilayer configuration. A smaller I_G/I_{2D} ratio suggests reduced carrier scattering via interlayer electron-phonon coupling. The generated results have indicated that coupling in turbostratic graphene does exist, albeit much smaller than that in exfoliated graphene, as reflected by the gradual increase in the I_G/I_{2D} ratio as layer number increases. Furthermore, the $FWHM_{2D}$ results for graphene/*h*-BN/graphene is 43 cm^{-1}, mimic those for monolayer graphene, indicating minimum impact between two monolayers.

3.2. Density-function-theory (DFT) simulation

The DFT simulation was conducted to study the *E-k* dispersion in graphene monolayer, *AB*-stacked bilayer, and graphene/*h*-BN/graphene heterostructure, as shown in Fig. 3a–d. While graphene/monolayer *h*-BN/graphene would be an ideal case, in our experiment 22 nm (65 layers) was the minimum thickness of *h*-BN flake that could be identified under the optical microscope used for making the structures. DFT calculations are performed with PBE functional [32] which is implemented by SIESTA [33]. DZP orbitals are used for C, B and N atoms. Initial structure is placed in a hexagonal lattice, and a 2-nm space is added to the graphene/*h*-BN/graphene structure to isolate the interaction between unit cells. Then, atoms are relaxed with force threshold of 0.01 eV/A. The relaxed structure has a lattice constant of 2.504 A. 11 × 11 × 1 Monkhorst-Pack grid is used in the calculation and Mesh cutoff is 300 Ry.

Linear *E-k* dispersion is seen in monolayer graphene (Fig. 3a) whereas bilayer graphene has multiple bands at the Dirac cone (Fig. 3b). Band splitting in bilayer graphene is the direct consequence of interlayer interaction which causes the Π and Π* bands to be divided. While the presence of heavy holes and electrons degrades carrier mobility, the split of conduction and valence bands

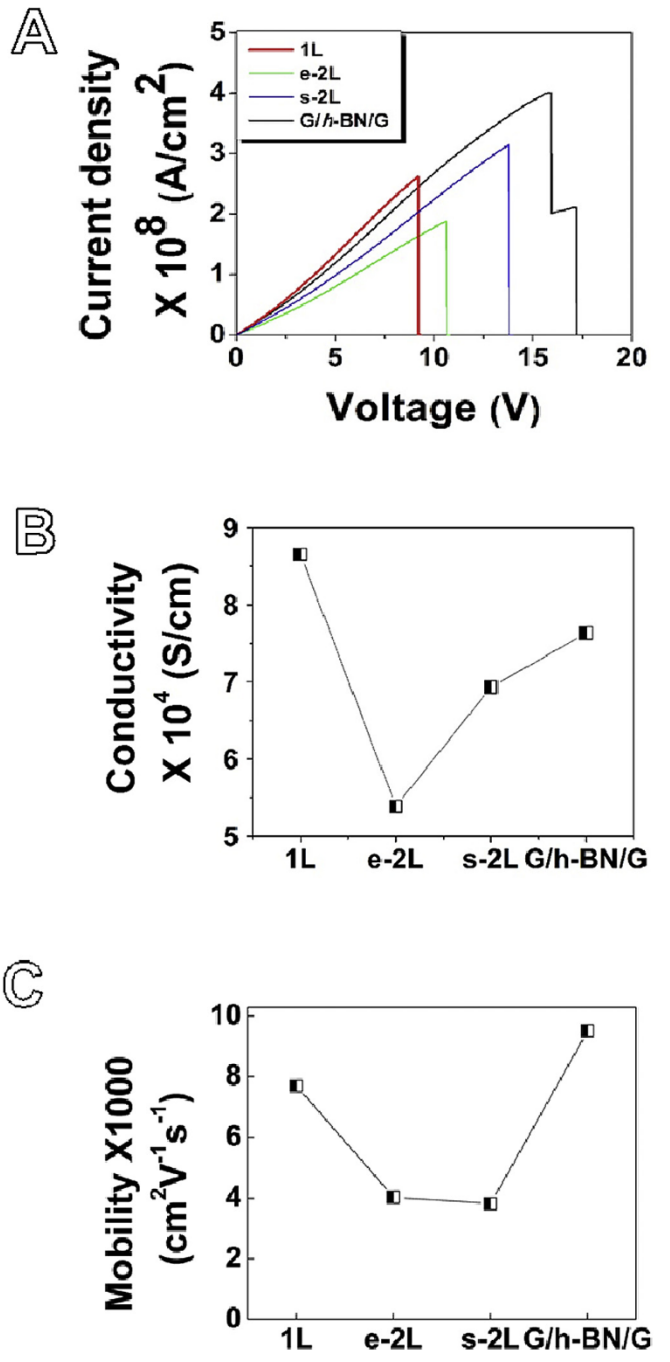


Fig. 4. **(a)** Measured electrical current density in structures with four different sample configurations, including monolayer graphene, exfoliated (*AB*-stacked) graphene, randomly-stacked bilayer graphene, and graphene/*h*-BN/graphene heterostructure. **(b) & (c)** Conductivity and mobility as measured in these different configurations respectively. (A colour version of this figure can be viewed online.)

into two sub-bands does not directly open up a bandgap, as the lower conduction sub-band and the higher valence sub-band are still degenerate at the Dirac point. However, degeneracy breaks under strong electric field in the perpendicular-to-plane direction, and sub-bands move away from each other, resulting in the opening of band gap [34].

As shown in Fig. 3c, the introduction of monolayer *h*-BN between two graphene layers helps to prevent band split, bringing back degeneracy. The observed linear dispersion mimics the one observed in monolayer graphene, confirming that carriers remain massless Dirac fermions. The DFT study confirm the presence of degeneracy in the graphene/65-layer *h*-BN/graphene heterostructure. It is inferred that in such a heterostructure, linear *E-k* dispersion is expected, similar to monolayer graphene. The result confirms the isolation of the two graphene monolayers, each behaving as independent conducting channel due to *h*-BN interposer. It must be noted that 22 nm is not an optimized thickness, rather the minimum thickness obtained while performing micromechanical exfoliation of *h*-BN. Other samples were created using flakes with thickness varying from 22 nm to 55 nm, and similar results were observed.

3.3. Electrical measurements

Fig. 4a shows the measured current density vs. voltage characteristics (in vacuum) of the four different sample configurations. The conductivity is shown for each sample (Fig. 4b). The monolayer graphene (red-color) serves as the reference. In exfoliated *AB*-stacked bilayer (green-color) the interlayer scattering is expected to be significant. It is noted that the current density in that sample is less than that in monolayer, despite doubled cross-sectional area (For instance, at 5 V, current is ~30% lower). The degraded conductivity in bilayer is the indication of interlayer scattering. For stacked bilayer (blue-color), improved conduction is observed as compared with exfoliated bilayer, confirming turbostratic graphene exhibits reduced scattering. However, current density in turbostratic graphene is much below the ideal value (monolayer), signifying degradation (Fig. 4b). Finally, the graphene/*h*-BN/graphene heterostructure is studied to understand the impact of *h*-BN interposer. It is noticed that current is improved from other structures with current density closer to the ideal value (monolayer), as shown in Fig. 4b.

Carrier mobility is measured as a function of ambient temperature. Monolayer graphene exhibits high mobility due to the fact that carriers mimic Dirac fermions. However, substrate is a limiting factor and a field-effect mobility of ~8000 $cm^2/V.s$ (room temperature) is measured for monolayer graphene (Fig. 4c). SiO_2 is known to have surface phonons with low energy (~55 meV) [35]. The phonons couple with carriers, resulting in degraded mobility. The effect, known as surface polar phonon scattering, is relevant in 2D systems, as carriers are present in the vicinity of a solid surface. Surface vibrations, arisen from abrupt termination of crystal lattice at surface, have lower energy in SiO_2 as compared with that in *h*-BN due to the surface-limiting nature in the latter. In bilayer graphene, the lower layer partially screens the top layer from the substrate phonon-induced field, however, the mobility value remains considerably lower than that of monolayer graphene (~3000 $cm^2/V{\cdot}s$) at room temperature. This is the direct result of interlayer scattering which causes reduction in carrier Fermi velocity. The stacked bilayer graphene fares only slightly better with the observed carrier mobility of ~3500 $cm^2/V{\cdot}s$ at room temperature. It should be noted that, when *h*-BN is used as an interposing layer, the decoupling between the two graphene monolayers causes an upswing in mobility. An approximate value of 9000 $cm^2/V{\cdot}s$ at room temperature was observed for double-layer graphene with interposing *h*-BN, the value being even higher than what was observed in a monolayer graphene. We attribute this enhancement to two key factors, decoupling of the two graphene monolayers and high mobility in the top graphene monolayer (attributed to the high-energy optical phonons in *h*-BN, which does not create enough polar phonon scattering on the surface). It has been shown in our prior work that graphene mobility is significantly enhanced as placed in contact with *h*-BN rather than SiO_2 [27]. The result confirms that electrical conduction (in terms of conductivity and carrier mobility) is improved in graphene/*h*-BN/graphene

heterostructure as compared with bilayer graphene (either stacked or exfoliated).

Interestingly the graphene/*h*-BN/graphene heterostructure has lower conductivity (at zero gate voltage) despite having higher mobility than monolayer graphene. Conductivity is given by,

$$\sigma = n^*q^*\mu$$

(σ – Conductivity, n – Carrier density, q – electronic change, and μ - carrier mobility).

Low conductivity (despite high mobility) arises due to the carrier density being lower in G/*h*-BN/G compared with monolayer graphene. The carrier density can be obtained using,

$$n = \varepsilon_r\varepsilon_0*(V_g - V_{Dirac})/t_{ox}$$

(t_{ox} – thickness of the oxide, ε_r – Relative permittivity of oxide substrate, ε_0 – permittivity of free space, Vg – Gate voltage, V_{Dirac} – Voltage at Dirac point).

At zero gate voltage, the carrier density, *n*, is a direct outcome of the amount of 'doping' in the graphene channel. This 'doping' is characterized by the voltage at Dirac point, V_{Dirac} as obtained from the transfer characteristics of graphene channel (R vs. V_g plot). Since this 'doping' is observed to be higher in monolayer graphene as compared to graphene/*h*-BN/graphene structure, the overall conductivity is compromised. The higher value of V_{Dirac} in monolayer graphene is an outcome of the higher degree of electrostatic interaction with the environment (substrate as well as air). For graphene/*h*-BN/graphene, *h*-BN provides one inert interface for both the graphene layers resulting in lower interfacial electrostatic interaction and correspondingly lower V_{Dirac} and lower carrier density. When the operating point is close to the Dirac point, the carrier density is low (case of G/*h*-BN/G since Dirac point is close to zero) and the conductivity approaches its minimum value when operating at Dirac point. Far away from the Dirac point, there is no electrostatic control of the gate on the channel, the result is lower resistance and higher conductivity (case of monolayer graphene).

4. Summary

We investigated conduction behavior in double-layered graphene system with interposing *h*-BN multilayer, a unit cell structure of the conceptual graphene/*h*-BN superlattice. Reduction of coupling between two graphene monolayers is observed. The linear dispersion at the Dirac point in Brillouin zone is seen in the graphene/*h*-BN/graphene heterostructure, reflected by the DTF simulation. Raman spectra confirm, via the existence of a single 2D peak, the electrical isolation of two graphene monolayers. This decoupling is well reflected in electrical behavior of the graphene/*h*-BN/graphene heterostructure in which improved conductivity and carrier mobility are observed with reference to *AB*-stacked bilayer graphene. The results indicate that the current-carrying capacity in multi-layered graphene could be significantly improved, to that of a pristine monolayer, by using thin *h*-BN as the interposer in the graphene multilayers. The graphene/*h*-BN superlattice, using the demonstrated trilayer heterostructure as a unit cell, shows promise as the next-generation high-performance conductors.

Competing financial interests

The authors declare no competing financial interests.

Acknowledgments

The authors would like to acknowledge funding supports from U.S. National Science Foundation (grant no. 1162312 and 1434689). N. J. thanks Michael Murphy for assistance with layer transfer for sample preparation and Tianhua Yu for fabrication. MPA was supported by the National Science Foundation through the Division of Electrical, Communications and Cyber Systems under Grant ECCS-1231927

References

[1] K.S. Novoselov, A.K. Geim, S.V. Morozov, D. Jiang, M.I. Katsnelson, I.V. Grigorieva, S.V. Dubonos, A.A. Firsov, Two-dimensional gas of massless dirac fermions in graphene, Nature 438 (2005) 197–200.
[2] A.H. Castro Neto, F. Guinea, N.M.R. Peres, K.S. Novoselov, A.K. Geim, The electronic properties of graphene, Rev. Mod. Phys. 81 (2009) 109–162.
[3] A.K. Geim, K.S. Novoselov, The rise of graphene, Nat. Mater. 6 (2007) 183–191.
[4] C. Lee, X. Wei, J.W. Kysar, J. Hone, Measurement of the elastic properties and intrinsic strength of monolayer graphene, Science 321 (2008) 385–388.
[5] G.-H. Lee, R.C. Cooper, S.J. An, S. Lee, A. van der Zande, N. Petrone, A.G. Hammerberg, C. Lee, B. Crawford, W. Oliver, et al., High-strength chemical-vapor–deposited graphene and grain boundaries, Science 340 (2013) 1073–1076.
[6] F. Scarpa, S. Adhikari, A.S. Phani, Effective elastic mechanical properties of single layer graphene sheets, Nanotechnology 20 (2009), 065709.
[7] B.D. Briggs, B. Nagabhirava, G. Rao, R. Geer, H. Gao, Y. Xu, B. Yu, Electromechanical robustness of monolayer graphene with extreme bending, Appl. Phys. Lett. 97 (2010), 223102.
[8] J.S. Bunch, A. M. van der Zande, S.S. Verbridge, I.W. Frank, D.M. Tanenbaum, J.M. Parpia, H.G. Craighead, P.L. McEuen, Electromechanical resonators from graphene sheets, Science 315 (2007) 490–493.
[9] K.S. Kim, Y. Zhao, H. Jang, S.Y. Lee, J.M. Kim, K.S. Kim, J.-H. Ahn, P. Kim, J.-Y. Choi, B.H. Hong, Large-scale pattern growth of graphene films for stretchable transparent electrodes, Nature 457 (2009) 706–710.
[10] R. Murali, Y. Yang, K. Brenner, T. Beck, J.D. Meindl, Breakdown current density of graphene nanoribbons, Appl. Phys. Lett. 94 (2009), 243114.
[11] K.-J. Lee, A.P. Chandrakasan, J. Kong, Breakdown current density of CVD-grown multilayer graphene interconnects, IEEE Electron. Device Lett. 32 (2011) 557–559.
[12] T. Yu, E.-K. Lee, B. Briggs, B. Nagabhirava, B. Yu, Bilayer graphene system: current-induced reliability limit, IEEE Electron. Device Lett. 31 (2010) 1155–1157.
[13] T. Yu, E. Kim, N. Jain, Y. Xu, R. Geer, B. Yu, Carbon-based interconnect: performance, scaling and reliability of 3D stacked multilayer graphene system, in: Electron Devices Meeting (IEDM), 2011 IEEE International, 2011, 7.5.1–7.5.4.
[14] E.V. Castro, K.S. Novoselov, S.V. Morozov, N.M.R. Peres, J.M.B.L. dos Santos, J. Nilsson, F. Guinea, A.K. Geim, A.H.C. Neto, Biased bilayer graphene: semiconductor with a gap tunable by the electric field effect, Phys. Rev. Lett. 99 (2007), 216802.
[15] Y. Sui, J. Appenzeller, Screening and interlayer coupling in multilayer graphene field-effect transistors, Nano Lett. 9 (2009) 2973–2977.
[16] J. Hass, F. Varchon, J.E. Millán-Otoya, M. Sprinkle, N. Sharma, W.A. de Heer, C. Berger, P.N. First, L. Magaud, E.H. Conrad, Why multilayer graphene on 4H-SiC (000$\bar{1}$) behaves like a single sheet of graphene, Phys. Rev. Lett. 100 (2008), 125504.
[17] M. Sprinkle, D. Siegel, Y. Hu, J. Hicks, A. Tejeda, A. Taleb-Ibrahimi, P. Le Fèvre, F. Bertran, S. Vizzini, H. Enriquez, et al., First direct observation of a nearly ideal graphene band structure, Phys. Rev. Lett. 103 (2009), 226803.
[18] S. Shallcross, S. Sharma, O.A. Pankratov, Quantum interference at the twist boundary in graphene, Phys. Rev. Lett. 101 (2008), 056803.
[19] R. Bistritzer, A.H. MacDonald, Transport between twisted graphene layers, Phys. Rev. B 81 (2010), 245412.
[20] J.M.B. Lopes dos Santos, N.M.R. Peres, A.H. Castro Neto, Graphene bilayer with a twist: electronic structure, Phys. Rev. Lett. 99 (2007), 256802.
[21] V. Perebeinos, J. Tersoff, P. Avouris, Phonon-mediated interlayer conductance in twisted graphene bilayers, Phys. Rev. Lett. 109 (2012), 236604.
[22] A. Luican, G. Li, A. Reina, J. Kong, R.R. Nair, K.S. Novoselov, A.K. Geim, E.Y. Andrei, Single-layer behavior and its breakdown in twisted graphene layers, Phys. Rev. Lett. 106 (2011), 126802.
[23] G. Trambly de Laissardiere, D. Mayou, L. Magaud, Localization of dirac electrons in rotated graphene bilayers, Nano Lett. 10 (2010) 804–808.
[24] C.R. Dean, A.F. Young, I. Meric, C. Lee, L. Wang, S. Sorgenfrei, K. Watanabe, T. Taniguchi, P. Kim, K.L. Shepard, et al., Boron nitride substrates for high-quality graphene electronics, Nat. Nano 5 (2010) 722–726.
[25] N. Jain, T. Bansal, C. Durcan, B. Yu, Graphene-based interconnects on hexagonal boron nitride substrate, IEEE Electron. Device Lett. 33 (2012) 925–927.
[26] E. Kim, N. Jain, R. Jacobs-Gedrim, Y. Xu, B. Yu, Exploring carrier transport phenomena in a CVD-assembled graphene FET on hexagonal boron nitride, Nanotechnology 23 (2012), 125706.
[27] N. Jain, C.A. Durcan, R. Jacobs-Gedrim, Y. Xu, B. Yu, Graphene interconnects fully encapsulated in layered insulator hexagonal boron nitride, Nanotechnology 24 (2013), 355202.
[28] Z. Zhang, F. Yang, P. Agnihotri, et al., Reverse degradation of nickel graphene

junction by hydrogen annealing, AIP Adv. 6 (2) (2016), 025301.
[29] L. Wang, I. Meric, P.Y. Huang, Q. Gao, Y. Gao, H. Tran, T. Taniguchi, K. Watanabe, L.M. Campos, D.A. Muller, et al., One-dimensional electrical contact to a two-dimensional material, Science 342 (2013) 614–617.
[30] A.C. Ferrari, J.C. Meyer, V. Scardaci, C. Casiraghi, M. Lazzeri, F. Mauri, S. Piscanec, D. Jiang, K.S. Novoselov, S. Roth, et al., Raman spectrum of graphene and graphene layers, Phys. Rev. Lett. 97 (2006), 187401.
[31] S. Latil, V. Meunier, L. Henrard, Massless fermions in multilayer graphitic systems with misoriented layers: *ab initio* calculations and experimental fingerprints, Phys. Rev. B 76 (2007), 201402.
[32] J.P. Perdew, K. Burke, M. Ernzerhof, Generalized gradient approximation made simple, Phys. Rev. Lett. 77 (1996) 3865.
[33] J.M. Soler, E. Artacho, J.D. Gale, A. García, J. Junquera, P. Ordejón, D. Sánchez-Portal, The *SIESTA* method for *ab-initio* order-N materials simulation, J. Phys. Condens. Matter. 14 (2002) 2745–2779.
[34] K.F. Mak, C.H. Lui, J. Shan, T.F. Heinz, Observation of an electric-field-induced band gap in bilayer graphene by infrared spectroscopy, Phys. Rev. Lett. 102 (2009), 256405.
[35] S. Fratini, F. Guinea, Substrate-limited electron dynamics in graphene, Phys. Rev. B 77 (2008) 19541.